J Ther Eng, Vol. 11, No. 3, pp. 845−857, May, 2025

Journal of Thermal Engineering
Web page info: https://jten.yildiz.edu.tr
DOI: 10.14744/thermal.0000950

Research Article

Numerical modelling of 3D magnetohydrodynamics chemically reacting permeable sheet influenced by free stream convection nanofluid flow

Smita YADAV[1], Sanjay KUMAR[2], Parmod Kumar SHARMA[2], Vinita MAKKAR[3], Khyati DANG[3,*]

[1]Department of Mathematics, RPS College, Haryana, 123029, India
[2]Department of Applied Sciences, KIET Group of Institutions, Uttar Pradesh, 201206, India
[3]Department of Basic and Applied Sciences, SoES, GD Goenka University, Haryana, 122103, India

ARTICLE INFO

Article history
Received: 29 February 2024
Revised: 11 October 2024
Accepted: 13 October 2024

Keywords:
Chemical Reaction; Magnetohydrodynamics; Nanofluid; Non-Newtonian Casson Fluid; Permeable Sheet

ABSTRACT

The effects of a chemical reaction on mixed convective nanofluid flow along a permeable stretched surface in the presence of free stream flow are demonstrated. The impact of multiple non-dimensional characteristics on different gradients and profiles is investigated. Through appropriate transformations, governing coupled partial differential equations become ordinary differential equations, which are then solved numerically. Through MATLAB programming, Runge Kutta Fehlberg method by following shooting technique yields the numerical solutions. Influence of fluid parameters especially free stream velocity, thermal Biot number, concentration Biot number, heat generation parameter, chemical reaction parameter, stretching ratio parameter, permeability parameter, magnetic parameter, Prandtl number, Brownian motion parameter, Lewis number has been investigated that makes this research novel one. The calculated results are presented in the form of tables and contour plots. Furthermore, examined are the thermal transfer strength (Nusselt number) and the mass exchange strength (Sherwood number). According to our research, the velocity distribution gets smaller as the magnetic parameter increases, but the corresponding profile gets increases for free stream velocity flow. With rise in the values of stretching ratio parameter from 2.0-10.0, heat transfer rate falls down by 7.24%. Heat transfer rate falls down by 22.37% with rise in the values of Prandtl number within the range 0.2-1.0. Additionally, temperature enhances with enhancement in thermal Biot number. Comparing its latest findings to prior outcomes and accomplishing convergence criteria supports this technique's validity. Current research in this domain has diverse applications, encompassing power plants, refrigeration systems, medical science, ranging from transportation to energy production and in wide variety of industries, Micro-Electro-Mechanical Systems and in the field of biotechnology. This research attempts to help industrial companies achieve product quality by regulating transport phenomena.

Cite this article as: Yadav S, Kumar S, Sharma PK, Makkar V, Dang K. Numerical modelling of 3D magnetohydrodynamics chemically reacting permeable sheet influenced by free stream convection nanofluid flow. J Ther Eng 2025;11(3):845−857.

***Corresponding author.**
*E-mail address: khyatidang43870@gmail.com

This paper was recommended for publication in revised form by Editor-in-Chief Ahmet Selim Dalkılıç

Published by Yıldız Technical University Press, İstanbul, Turkey
Yıldız Technical University. This is an open access article under the CC BY-NC license (http://creativecommons.org/licenses/by-nc/4.0/).

INTRODUCTION

Researchers are paying closer attention to nanofluid because of its unique physical characteristics and wide range of uses, particularly in the manufacturing, industrial, and biomedical sectors. Nanofluids are the most appropriate coolants in the aforementioned specific uses due to their increased heat conductivity. Choi and Eastman [1] introduced nanofluids to address the aforementioned significant concern. Nanofluids are defined as a blend of conventional fluids with Nanoscale particles (metals, metal oxides, etc.) that have superior heat transmission properties. Because nanofluids have noticeably better thermal conductivities, they function well as coolants in different zones. Computers, nuclear reactors, surgery, treatment of chronic illnesses, various microelectronic devices, cars, and transformers are a few examples of these application sectors [2-7]. Nagaraja et al. [8] expresses impact of conveying ternary hybrid nanofluid radiative flow in presence of aiding flow conditions by applying shooting algorithm. Influence of heat radiation and thermophoretic deposition by following RKF (Runge Kutta Fehlberg) technique has been reported by Karthik et al. [9] across wedge and shows that mass transfer rate declines because of enhancement in solid volume fraction. Reddy et al. [10] uses FEM (Finite Element Method) technique to study slip effects in presence of suction utilizing Al_2O_3 & TiO_2 hybrid nanoparticles and presented that with rise in volume fraction of Al_2O_3 & TiO_2, temperature rises up. Asalekar et al. [11] discussed the influence of vegetable nanofluids induced by novel hybrid nanoparticles by utilizing ANN prediction. Mebarek-Oudina et al. [12] discussed the magnetite-water fluid flow. Sheikholeslami and Khalili [13] presented numerical simulation for spectral splitter induced by nanofluids. Jayadevamurthy et al. [14] studied the bioconvective flow induced by rotating disc utilizing unsteady fluid flow. Sepehrnia et al. [15] discussed dynamic viscosity & sensitivity analysis based on Sio_2 / *MWCNT*.

The extensive industrial and engineering uses of Casson fluids have drawn more attention to their study. All of these commonly used goods have one thing in common: they are indifferent to Newton's law of viscosity. As a result, these liquids are well known for not being Newtonian. When β is the Casson parameter, the Casson fluid has limiting features (non-Newtonian fluidity) that reflect infinite viscosity at zero shear stress $\beta \to 0$ and Newtonian viscosity at enormous stress $\beta \to \infty$. This is the unique quality that Casson fluid has. When shear tension and small shear strain exceed a threshold, the behavior of Casson fluid is similar to that of a flexible solid. Alqahtani et al. [16] utilizing HAM (Homotopy Analysis Method) algorithm to study impact of Al_2O_3 & *Cu* hybrid nanoparticles in presence of Darcy effects induced via exponential sheet. Puneeth et al. [17] studied influence of non-Newtonian nanofluid flow along with gyrotactic microorganisms flowing between diverging channels utilizing FEM & by applying similarity transformation. Akaje et al. [18] utilizing Spectral Collocation Method to analyze analytically influence of chemical reaction & MHD Casson nano liquids and shows that with increase in Soret effects, concentration distribution rises up. Seethamahalakshmi et al. [19] reported impact of convection heating and slip flow induced by Maxwell nanofluid over porous surface.

The look at of the drift of electrically carrying out fluids in a regular or fluctuating magnetic Field (MF) is referred to as magnetohydrodynamics (MHD). Many uses for MHD have been discovered, including the transportation of subterranean species, improved oil recovery, medicine, biology, geothermal reservoirs, refrigeration systems, and encompassing power plants, among many more. Lund et al. [20] utilizing the bvp4c approach to study thermal radiation impact induced by Al_2O_3 - *Cu*/*SA* hybrid Casson nanofluids with MHD flow over permeable surface. Ali et al. [21] expressed impact of hydromagnetic flow in addition to thermal radiation induced via stretching surface and calculated results by utilizing Tecplot-360 software. Influence of activation energy in presence of MHD Casson nanofluid flow over exponential surface under the impact of Hall current by using MATLAB bvp4c package has been presented by Kumar et al. [22]. In recent years, MHD nanofluid flow has been addressed in [23, 24]. Gaseous modelling combustion utilizing species transport approach has been presented by Rajak et al. [25]. Rajak et al. [26] discussed diesel engine characteristics by following 3D CFD numerical approach.

This model garnered significant attention from scientists because of distinctive characteristics and considerable potential applications. It has diverse applications, encompassing power plants, refrigeration systems, medical science, and other fields. The goal of the current work is to investigate how chemical reactions affect the flow of free stream MHD nanofluids when heat convection occurs across a permeable surface. The study extensively analyzes and discusses the distinct behaviors of flow velocity, fluid temperature, and nanoparticle concentration in response to various critical physical parameters makes this research novel one. The dimensionless basic differential equation systems were computationally solved using the MATLAB software and the computational RKF technique by using the ODE45 solver. The current study's distinctive findings are beneficial and relevant for academic research as well as other fields.

MATHEMATICAL FORMULATION

The 3D model under consideration includes nanofluid MHD flow, heat production, and chemical reaction embedded in a permeable sheet with concentration and thermal Biot numbers (Fig. 1). Where a and b are constants, flow is constrained at $z \geq 0$ and positioned between stretching velocities $U_w = ax$ & $V_w = by$ *at* $z = 0$ at $z = 0$. Considered physical problem is analyzed with the below adopted assumptions:

- Free stream velocity flow
- Boundary layer Problem
- Reynolds number
- Heat radiation
- Thermal Diffusion

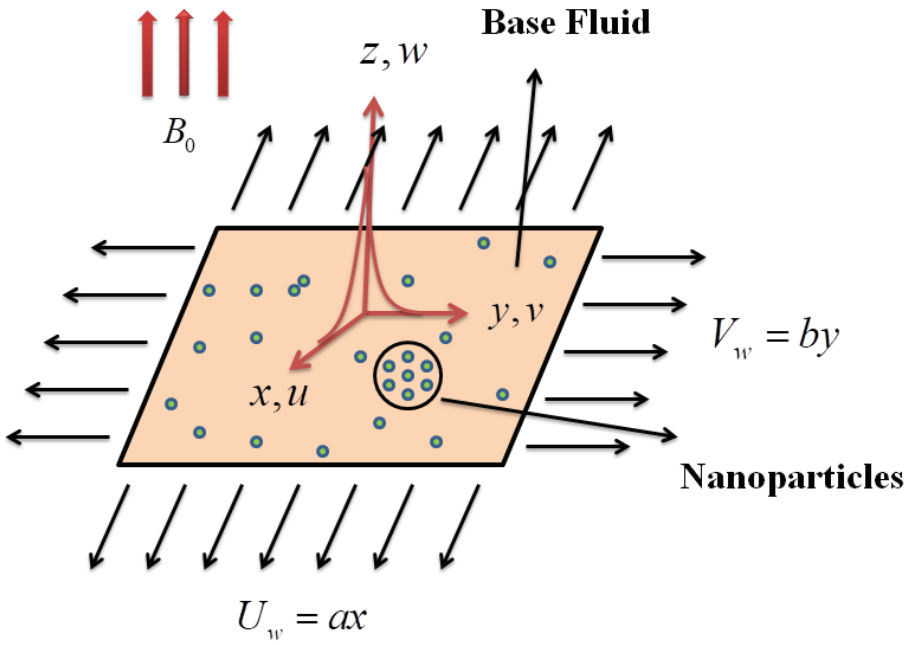

Figure 1. Physical diagram.

The considered governing equations are [2, 27, 28]:

$$\frac{\partial u}{\partial x}+\frac{\partial v}{\partial y}+\frac{\partial w}{\partial z}=0 \tag{1}$$

$$u\frac{\partial u}{\partial x}+v\frac{\partial u}{\partial y}+w\frac{\partial u}{\partial z}=\nu\frac{\partial^2 u}{\partial z^2}+U_\infty\frac{\sigma B_0^2}{\rho}+U_\infty\frac{\partial U_\infty}{\partial z}-\left[\frac{\sigma B_0^2}{\rho}+\frac{\nu}{k_1}\left(1+\frac{1}{\beta}\right)\right]u \tag{2}$$

$$u\frac{\partial v}{\partial x}+v\frac{\partial v}{\partial y}+w\frac{\partial v}{\partial z}=\nu\frac{\partial^2 v}{\partial z^2}+U_\infty\frac{\sigma B_0^2}{\rho}+U_\infty\frac{\partial U_\infty}{\partial z}-\left[\frac{\sigma B_0^2}{\rho}+\frac{\nu}{k_1}\left(1+\frac{1}{\beta}\right)\right]v \tag{3}$$

$$u\frac{\partial T}{\partial x}+v\frac{\partial T}{\partial y}+w\frac{\partial T}{\partial z}=\frac{k_1}{(\rho C_p)_f}\frac{\partial^2 T}{\partial z^2}+\frac{(\rho C_p)_p}{(\rho C_p)_f}\left[\frac{D_T}{T_\infty}\left(\frac{\partial T}{\partial z}\right)^2+D_B\frac{\partial T}{\partial z}\frac{\partial C}{\partial z}\right]-\frac{1}{(\rho C_p)_f}\frac{\partial q_r}{\partial z} \tag{4}$$

$$u\frac{\partial C}{\partial x}+v\frac{\partial C}{\partial y}+w\frac{\partial C}{\partial z}=\frac{D_T}{T_\infty}\frac{\partial^2 T}{\partial z^2}+D_B\frac{\partial^2 C}{\partial z^2}-K_r(C-C_\infty) \tag{5}$$

Where u, v and w denotes the velocity components along x, y and z direction respectively. Also, σ denotes electrical conductivity, β denotes Casson fluid parameter, ν denotes kinematic viscosity, B_0 denotes magnetic field intensity, ρ denotes density of fluid, U_∞ denotes stream velocity, k_1 denotes thermal conductivity, T denotes temperature, $(\rho C_p)_p$ denotes heat capacity at constant pressure, C denotes concentration, C_∞ denotes ambient concentration, D_T denotes thermophoretic diffusion coefficient, K_r denotes dimensionalized chemical reaction, $(\rho C_p)_f$ denotes heat capacity of the fluid, T_∞ denotes ambient temperature, D_B denotes Brownian diffusion coefficient..

Using similarity variables [29]:

$$\zeta=\sqrt{\frac{a}{\nu}}z,\ \Theta(\zeta)=\frac{T-T_\infty}{T_w-T_\infty},\ \Phi(\zeta)=\frac{C-C_\infty}{C_w-C_\infty},\ u=axf'(\zeta),\ v=byg'(\zeta)\ and\ w=-\sqrt{a\nu[f(\zeta)+cg(\zeta)]} \tag{6}$$

Where, ζ denotes similarity variables, a & b denotes constants, Θ denotes temperature distribution, Φ denotes concentration distribution, T_w & C_w are the temperature and concentration at wall serially and c denotes stretching ratio parameter.

Associated B.C's are:

$$u=U_w=ax,\quad v=V_w=by\quad at\quad w=0,\quad -k_f\left(\frac{\partial T}{\partial z}\right)=h_f(T_w-T),\ -D_B\left(\frac{\partial T}{\partial z}\right)=h_s(C_w-C)\ at\ z=0,\quad u\to 0,\ v\to 0,\ T\to T_\infty,\ C\to C_\infty\ as\ z\to\infty \tag{7}$$

Transformed D.E's are as follows:

$$\left(1+\frac{1}{\beta}\right)f'''-f'^2-M(f'-\lambda)+\lambda^2+(f+cg)f''-\left[M+PR\left(1+\frac{1}{\beta}\right)\right]f'=0 \tag{8}$$

$$\left(1+\frac{1}{\beta}\right)g'''-cg''^{2}-M(g'-\lambda)+\lambda^{2} + (f+cg)g''-\left[M+PR\left(1+\frac{1}{\beta}\right)\right]g'=0 \quad (9)$$

$$\Theta''+Pr\left[(f+cg)\Theta'+Nb\Theta'\Phi'+Nt\Theta'^{2}+Q\Theta\right]=0 \quad (10)$$

$$\Phi''+LePr(f+cg)\Phi'+\left(\frac{Nt}{Nb}\right)\Theta''-LePrCR\Phi=0 \quad (11)$$

Where, M denotes magnetic parameter, PR denotes permeability parameter, λ denotes free stream velocity, Le denotes Lewis number, Pr denotes Prandtl number, Nb denotes Brownian motion, CR denotes chemical reaction, Q denotes heat source parameter and Nt denotes thermophoresis parameter.

Reduced B.C's are:

$$f'=1,\ g'=1,\ \Theta'(\zeta)=-TB(1-\Theta(\zeta)),\quad \Phi'(\zeta)=-CB\left(1-\Phi(\zeta)\right),\quad f'\to 0,\ \ g'\to 0,\ \ \Theta\to 0,\ \ \Phi\to 0 \quad (12)$$

Where, TB & CB denotes thermal and concentration Biot numbers respectively. Also non-dimensionalized fluid parameters are symbolically represented as follows:

$$\beta=p\frac{\mu_B}{p_z}\sqrt{2\pi_c},\ M=\frac{\sigma {B_0}^2}{a\rho},\ Pr=\frac{\nu\rho C_p}{k},\ Nb=\frac{\tau D_B(C_w-C_\infty)}{\nu},\ Le=\frac{\alpha}{D_B},\ CB=\frac{h_s}{\sqrt{\frac{a}{\nu}}D_B},\ Nt=\frac{\tau D_T(T_w-T_\infty)}{\nu T_\infty},\ TB=\frac{h_f}{\sqrt{\frac{a}{\nu}}k_f} \quad (13)$$

Non-dimensionalized physical quantities are as follows:

$$Sh_x=\frac{-x}{(C_w-C_\infty)}\left(\frac{\partial C}{\partial z}\right)|_{z=0},\ Nu_x=\frac{-x}{(T_w-T_\infty)}\left(\frac{\partial T}{\partial z}\right)|_{z=0},\quad Cf_y=\frac{\tau_{yz}}{\rho U_w^2},\ \ Cf_x=\frac{\tau_{xz}}{\rho U_w^2} \quad (14)$$

$$Sh_x\,Re_x^{-1/2}=-\Phi'(0),\ Nu_x\,Re_x^{-1/2}=-\Theta'(0),\quad Cf_y\,Re_x^{1/2}=\left(1+\frac{1}{\beta}\right)g''(0),\ Cf_x\,Re_x^{1/2}=\left(1+\frac{1}{\beta}\right)f''(0), \quad (15)$$

Here Re_x is local Reynolds number.

Numerical Scheme

The MATLAB R2014a ODE45 solver and the RKF method are used to mathematically handle the arrangement of D.E.'s (8)–(11) with B.C.'s (12) (Fig. 2). Next, ten first-order D.E.s are created from these circumstances as

$$\tilde{r}(1)'=\tilde{r}(2) \quad (16)$$

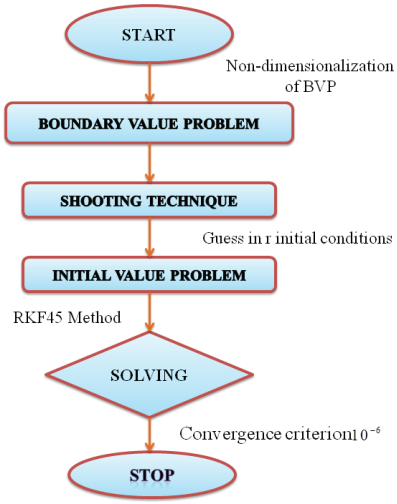

Figure 2. Numerical modelling flow chart.

$$\tilde{r}(2)'=\tilde{r}(3) \quad (17)$$

$$\tilde{r}(3)'=\frac{\beta}{(1+\beta)}\left[\tilde{r}(2)^2-\{\tilde{r}(1)+c\tilde{r}(4)\}\tilde{r}(3)+M\tilde{r}(2)+K_1\left(1+\frac{1}{\beta}\right)\tilde{r}(2)\right] \quad (18)$$

$$\tilde{r}(4)'=\tilde{r}(5) \quad (19)$$

$$\tilde{r}(5)'=\tilde{r}(6) \quad (20)$$

$$\tilde{r}(6)'=\frac{\beta}{(1+\beta)}\left[c\tilde{r}(5)^2-\{\tilde{r}(1)+c\tilde{r}(4)\}\tilde{r}(6)+M\tilde{r}(5)+\beta K_1\left(1+\frac{1}{\beta}\right)\tilde{r}(5)\right] \quad (21)$$

$$\tilde{r}(7)'=\tilde{r}(8) \quad (22)$$

$$\tilde{r}(8)'=-Pr[\{\tilde{r}(1)+c\tilde{r}(4)\}\tilde{r}(8)+Nb\tilde{r}(8)\tilde{r}(10)+Nt\tilde{r}(8)^2] \quad (23)$$

$$\tilde{r}(9)'=\tilde{r}(10) \quad (24)$$

$$\tilde{r}(10)'=-LePr\{\tilde{r}(1)+c\tilde{r}(4)\}\tilde{r}(10)-\left(\frac{Nt}{Nb}\right)\tilde{r}(8)' \quad (25)$$

Where

$$f=\tilde{r}(1),\ f'=\tilde{r}(2),\ f''=\tilde{r}(3),\ f'''=\tilde{r}(3)'\quad g=\tilde{r}(4),\ g'=\tilde{r}(5),\ g''=\tilde{r}(6),\ g'''=\tilde{r}(6)'\quad \Theta=\tilde{r}(7),\ \Theta'=\tilde{r}(8),\ \Theta''=\tilde{r}(8)'\quad \Phi=\tilde{r}(9),\ \Phi'=\tilde{r}(10),\ \Phi''=\tilde{r}(10)' \quad (26)$$

RESULTS AND DISCUSSION

In current analysis, results are compared along with residual error for different *Pr* as shown via Table 1. Table 2-4 presents values for $f''(0)$ & $g''(0)$, $-\theta'(0)$ and $\Phi'(0)$ for fixed entries of controlling fluid parameters as $\lambda = 0.1$ (Free stream velocity), $CB = 0.3$ (Concentration Biot number), $Q = 0.5$ (Heat generation parameter), $Cr = 0.6$ (Chemical reaction parameter), $c = 2.0$ (Stretching ratio parameter), $PR = 0.1$ (Permeability parameter), $\beta = 0.1$ (Casson fluid parameter), $M = 2.5$ (Magnetic parameter), $Pr = 0.73$ (Prandtl number), $Nb = 0.2$ (Brownian motion parameter), $Nt = 0.5$ (Thermophoresis parameter), $Le = 2.0$ (Lewis number), $TB = 0.1$ (Thermal Biot number).

The velocity distribution variation $g'(\zeta)$ against the parameter *PR* in the range of 0.05-0.10 is shown via Figure 3(a). This graph demonstrates how the velocity augmented somewhat when *PR* increases because there is more nanofluid present farther from the boundary, indicating a decrease in the thickness of the boundary layer and consequently, $g''(0)$ drops down from -0.819938652677649 to -0.849485482650904. The velocity distribution under the influence of λ ($0.10 \le \lambda \le 0.15$) is visualized in Figure 3(b). It was demonstrated that the velocity distribution and the free stream velocity parameter were closely proportional. As a result, when the free stream's velocity increases, the velocity distribution also increases and eventually decreases as it gets closer to the sheet's surface. The velocity distribution variation $g'(\zeta)$ against parameter *M* in the range of 0.1-0.5 as visualized in Figure 3(c). This graph demonstrates how the generated Lorentz drag force causes the velocity profile to fall gradually with little variation as the values of *M* increase. Furthermore, as Figure 3(c) illustrates, it has been observed that the width and magnitude of the boundary layer of $g'(\zeta)$) decrease with an increase in M and simultaneously $g''(0)$ declines from -0.574546600126926 to -0.628849145452216.

Table 1. A comparison for local Nusselt number with Hussain et al. [30], Wang [31] and Mabood et al. [32] along with residual error for different *Pr*

Pr	Hussain et al. [30]	Residual error	Wang [31]	Residual error	Mabood et al. [32]	Residual error	Present result
2	0.9114	0.0000	0.9114	0.0000	0.9114	0.0000	0.9114
20	3.3538	-0.0001	3.3539	0.0000	3.3539	0.0000	3.3539
70	6.4621	-0.0001	6.4622	0.0000	6.4622	0.0000	6.4622

Table 2. Values of $f''(0)$ & $g''(0)$ for *PR* ($0.05 \le Pr \le 0.10$), $\lambda(0.10 \le \lambda \le 0.15)$ and *M* ($0.1 \le M \le 0.5$)

PR	λ	*M*	$f''(0)$	$g''(0)$
0.05	0.1	2.5	-0.777562025003942	-0.819938652677649
0.06	-	-	-0.784027644062844	-0.825920032046307
0.07	-	-	-0.790437876636590	-0.831865171691975
0.08	-	-	-0.796794192480612	-0.837774284907418
0.09	-	-	-0.803097995277020	-0.843647625792008
0.10	-	-	-0.809350626966072	-0.849485482650904
0.10	0.10	-	-0.809350626966072	-0.849485482650904
-	0.11	-	-0.806053793697922	-0.846480230407608
-	0.12	-	-0.802733021389691	-0.843455469273812
-	0.13	-	-0.799388321229795	-0.840411240406145
-	0.14	-	-0.796019704340752	-0.837347584780535
-	0.15	-	-0.792627182389335	-0.834264543020026
-	0.10	0.1	-0.511734517510804	-0.574546600126926
-	-	0.2	-0.527565224517534	-0.588618649457148
-	-	0.3	-0.542920574463810	-0.602341598180555
-	-	0.4	-0.557841369945768	-0.615743622955963
-	-	0.5	-0.572363162343344	-0.628849145452216

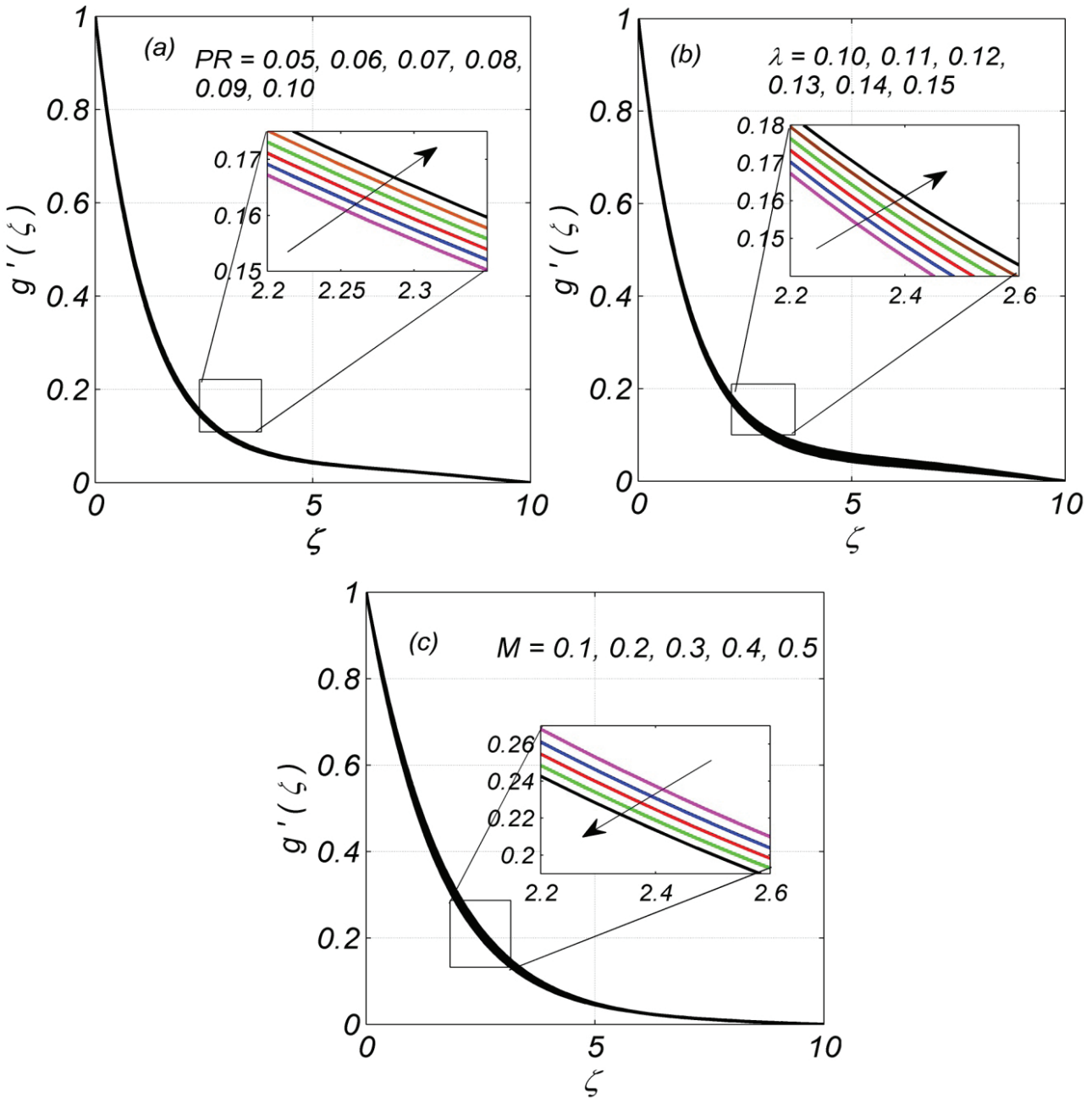

Figure 3. Velocity profile $g'(\xi)$ in direction of y-axis against (a) PR ($0.05 \leq PR \leq 0.10$), (b) λ ($0.10 \leq \lambda \leq 0.15$) and (c) M ($0.1 \leq M \leq 0.5$).

The temperature distribution's influence on the fluid parameters TB, c, Nb, Nt, Pr and Q are shown serially in Figures 4(a)-4(f). The temperature profile fluctuation against TB ($0.1 \leq TB \leq 0.9$) is explained in Figure 4(a), where it is observed that temperature and convection heating rising for higher TB. Additionally, graphs diverge for $0.0 \leq \zeta < 3.5$ (approximately), and then converge with $\zeta \rightarrow \infty$ beyond that. Furthermore, when TB fluctuates between 0.1 and 0.9, the Nusselt number decreases in the range of -0.088541536369859 to -0.395288634252507 as shown on Table 3. The impact of stretching ratio parameter c ($2.0 \leq c \leq 10.0$) on the temperature profile is seen in Figure 4(b). It is noted that the temperature distribution decays with an increase in stretching ratio parameter c. Figure 4(c) shows the fluctuation in $\Theta(\zeta)$ for different levels of Nb. Plotting $\Theta(\zeta)$ against growing Nb ($1.0 \leq Nb \leq 9.0$) yields maximum values, as demonstrated. Higher Nb values physically result in thicker thermal barrier layers, which raise temperature.

Table 3. Values of -$\Theta'(0)$ for TB ($0.1 \le TB \le 0.9$), c ($2.0 \le c \le 10.0$), Nb ($1.0 \le Nb \le 9.0$), Nt ($2.0 \le Nt \le 10.0$), Pr ($0.2 \le Pr \le 1.0$) and Q ($0.50 \le Q \le 1.50$)

TB	*c*	*Nb*	*Nt*	*Pr*	*Q*	-*Θ'*(0)
0.1	-	-	-	-	-	-0.088541536369859
0.3	-	-	-	-	-	-0.213904573511549
0.5	-	-	-	-	-	-0.296270136755862
0.7	-	-	-	-	-	-0.353538526151873
0.9	-	-	-	-	-	-0.395288634252507
-	2.0	-	-	-	-	-0.088541536376948
-	4.0	-	-	-	-	-0.092001343241164
-	6.0	-	-	-	-	-0.093483180597698
-	8.0	-	-	-	-	-0.094358344812766
-	10.0	-	-	-	-	-0.094953277965069
-	-	1.0	-	-	-	-0.087838005568556
-	-	3.0	-	-	-	-0.085846807677212
-	-	5.0	-	-	-	-0.083472797171521
-	-	7.0	-	-	-	-0.080643887962360
-	-	9.0	-	-	-	-0.077277950779695
-	-	-	2.0	-	-	-0.087728386458071
-	-	-	4.0	-	-	-0.086408477151171
-	-	-	6.0	-	-	-0.084677623243749
-	-	-	8.0	-	-	-0.082202020978397
-	-	-	10.0	-	-	-0.077875785228704
-	-	-	-	0.2	-	-0.073790700885929
-	-	-	-	0.4	-	-0.083609738138639
-	-	-	-	0.6	-	-0.087171204283452
-	-	-	-	0.8	-	-0.089119214400947
-	-	-	-	1.0	-	-0.090385039176517
-	-	-	-	-	0.50	-0.088541536376948
-	-	-	-	-	0.75	-0.086797493264815
-	-	-	-	-	1.00	-0.083979227817648
-	-	-	-	-	1.25	-0.078364642304093
-	-	-	-	-	1.50	-0.057225475769505

Similarly, as shown in Figure 4(d), raising the dimensionless thermophoresis parameter Nt ($2.0 \le Nt \le 10.0$) causes the thermophoretic force to become stronger. The impact of Nt on the dimensionless temperature profiles is shown in Figure 4(d). It has been noted that when Nt values rise, so does the temperature profile.

The relationship between Pr and $\Theta(\xi)$ is seen in Figure 4(e). The dimensionless curves indicate that at increased Pr ($0.2 \le Pr \le 1.0$), $\Theta(\zeta)$ decreased. In actuality, there is an inverse relationship between thermal diffusivity and Prandtl number. Less thermal diffusivity results from an increase in Pr, which causes a decline in the curves as visualized in Figure 4(e) and simultaneously Nusselt number drops down from -0.073790700885929 to -0.090385039176517. The variance in $\Theta(\zeta)$ for five distinct values of Q as 0.50, 0.75, 1.00, 1.20, and 1.50 is shown in Figure 4(f). When Q varies between 0.50 and 1.50, an increase in Q raises the fluid's temperature due to heat production via the heat source technique and the Nusselt number mounted in the range -0.088541536376948 to -0.057225475769505.

The influence of concentration distribution against the fluid parameters CB, CR, Le, Nb, and Nt serially is shown in

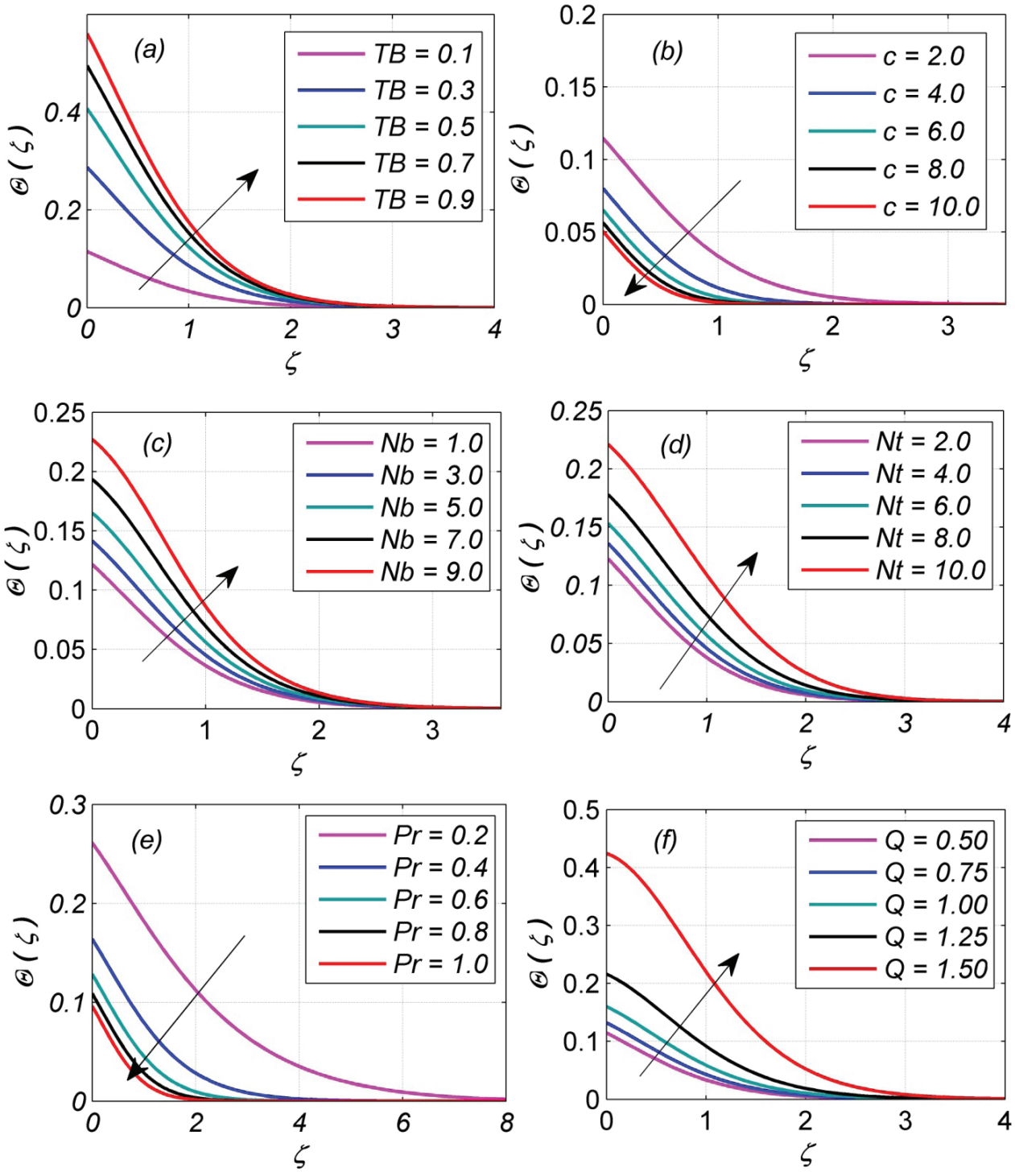

Figure 4. Temperature distribution against (a) *TB* ($0.1 \le TB \le 0.9$), (b) *c* ($2.0 \le c \le 10.0$), (c) *Nb* ($1.0 \le Nb \le 9.0$), (d) *Nt* ($2.0 \le Nt \le 10.0$), (e) *Pr* ($0.2 \le Pr \le 1.0$) and (f) *Q* ($0.50 \le Q \le 1.50$).

Figures 5(a)-5(e). Increase in concentration for greater *CB* ($0.2 \le CB \le 1.0$) values has been observed, is in fact visualized in Figure 5(a) and simultaneously, -*Φ*'(0) falls down from -0.172359090691536 to -0.612039859732770. Influence of chemical reaction *CR* ($0.5 \le CR \le 2.5$) on the distribution of nanoparticle concentrations is shown in Figure 5(b). It demonstrates that when the *CR* values increase, the concentration of nanoparticles drops. It takes place as a result

Table 4. Values of -$\Phi'(0)$ for CB ($0.2 \le CB \le 1.0$), CR ($0.5 \le CR \le 2.5$), Le ($1.5 \le Le \le 3.5$), Nb ($0.1 \le Nb \le 0.5$) and Nt ($1.0 \le Nt \le 5.0$)

CB	*CR*	*Le*	*Nb*	*Nt*	-$\Phi'(0)$
0.2	2.0	0.1	0.7	-	-0.172359090691536
0.4	-	-	-	-	-0.312804838685243
0.6	-	-	-	-	-0.429451162499494
0.8	-	-	-	-	-0.527875862277950
1.0		-	-	-	-0.612039859732770
-	0.5	-	-	-	-0.244440418143198
-	1.0	-	-	-	-0.251216249067726
-	1.5	-	-	-	-0.256160678776565
-	2.0		-	-	-0.259937729062749
-	2.5		-	-	-0.262925577508415
-	-	1.5	-	-	-0.236868031733801
-	-	2.0	-	-	-0.245990142265586
-	-	2.5		-	-0.252175904705804
-	-	3.0		-	-0.256708386246913
-	-	3.5		-	-0.260205066077814
-	-	-	0.1	-	-0.235663312096621
-	-	-	0.2	-	-0.245990142265586
-	-	-	0.3	-	-0.249433048679584
-	-	-	0.4	-	-0.251154979840411
-	-	-	0.5	-	-0.252188524353747
-	-	-	-	1.0	-0.236618805866993
-	-	-	-	2.0	-0.220094529005258
-	-	-	-	3.0	-0.206833023936196
-	-	-	-	4.0	-0.197284577613528
-	-	-	-	5.0	-0.192035907472882

of a decrease in molecule diffusivity with increasing CR and consequently, -$\Phi'(0)$ decreases from -0.244440418143198 to -0.262925577508415. The effect of Lewis number Le ($1.5 \le Le \le 3.5$) on the distribution of nanoparticle concentrations is seen in Figure 5(c). It is observed that as Le values increase, the distribution of nanoparticle concentrations diminishes. Physically, a higher Lewis number causes the nanofluids mass diffusivity to decrease, which aids in lowering the concentration and, ultimately, the concentration of the nanoparticles. Figures 5(d) and 5(e) show concentration distribution for the greater values of the Nb ($0.1 \le Nb \le 0.5$) and Nt ($1.0 \le Nt \le 5.0$) respectively. It indicates that the concentration declines for higher Brownian motion parameter, whereas the thermophoresis parameter exhibits obverse behavior. Furthermore, when Nb fluctuates between 0.1 and 0.5, the Sherwood number decreases in the range of -0.235663312096621 to -0.252188524353747.

The skin friction coefficient is shown using contour plots against the computational fluid parameters TB & Pr, Nt & CB, Nt & Le, and Nt & Pr, respectively, in Figures 6(a)-6(d). Figure 6(a) elaborates the change in skin friction against thermal Biot numbers TB ($0.00 \le TB \le 1.50$) and Prandtl numbers Pr ($0.00 \le Pr \le 1.50$). This contour plot illustrates that skin friction increases as TB and Pr increases. The contour plot of skin friction across the thermophoresis parameter Nt ($0.00 \le Nt \le 1.50$) and concentration Biot number CB ($0.00 \le CB \le 2.50$) as visualized in Figure 6(b), and it indicates that skin friction increases as both Nt and CB increase. Similarly, as can be seen in Figures 6(c), the contour plots provided via them demonstrate that skin friction increased with larger Nt & Le and Figure 6(d) shows skin friction increases when Nt ($0.00 \le Nt \le 1.50$) rises and Pr ($0.00 \le Pr \le 1.50$) falls.

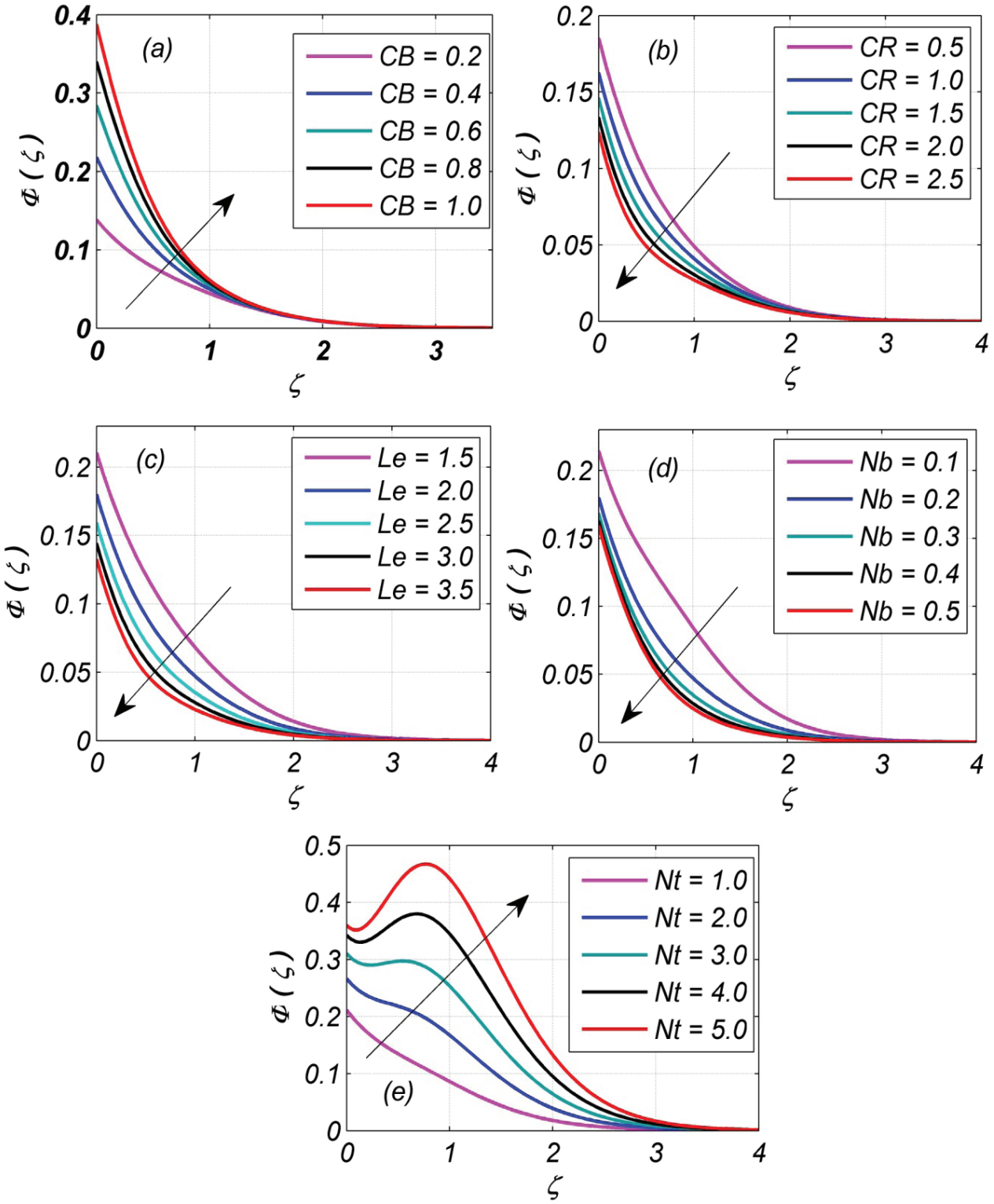

Figure 5. Concentration distribution against (a) *CB* ($0.2 \le CB \le 1.0$), (b) *CR* ($0.5 \le CR \le 2.5$), (c) *Le* ($1.5 \le Le \le 3.5$), (d) *Nb* ($0.1 \le Nb \le 0.5$) and (e) *Nt* ($1.0 \le Nt \le 5.0$).

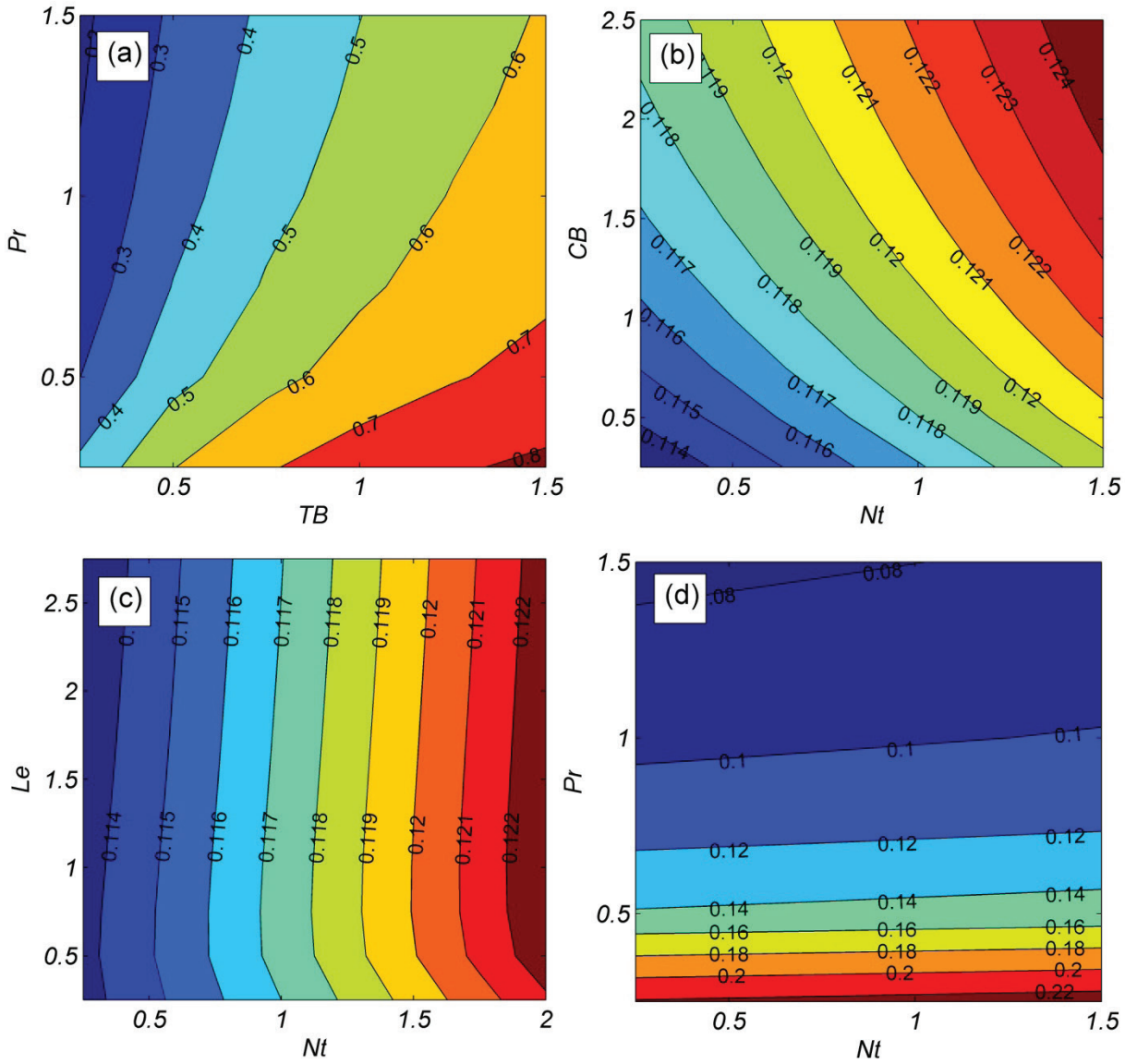

Figure 6. Skin friction coefficient against (a) *TB* & *Pr*, (b) *Nt* & *CB*, (c) *Nt* & *Le* and (d) *Nt* & *Pr*.

CONCLUSION

The transformation of partial differential equations into ordinary differential equations is accomplished by the use of similarity conversion. Final results include the temperature distribution, volume fraction of nanoparticles, Magnetohydrodynamics Casson nanofluid flow and the importance of Biot numbers. Final outcomes are as follows:

1. Intensification in concentration has been noticed out for higher concentration Biot number while concentration falls down for greater chemical reaction, Lewis number as well as Brownian motion.
2. Augmentation in the values of thermal Biot number, Brownian motion, thermophoresis and heat generation helps to increases temperature distribution. On the other hand, temperature declines with the increase in values of stretching ratio parameter and Prandtl number.
3. Higher stretching ratio parameter ranging from 2.0-10.0 leads to falls down heat transfer rate by 7.24%.
4. With rise in the values of Prandtl number from 0.2 to 1.0, heat transfer rate falls down by 22.37%.
5. Velocity declines against higher magnetic parameter due to Lorentz drag force.
6. Inclination in velocity is observed for greater permeability parameter and free stream velocity parameter.
7. Skin friction coefficient rises up with simultaneous augmentation in thermal Biot number and Prandtl number.

The results of this study are useful for controlling the heat transfer rate and fluid velocity in various industrial

applications, biochemical systems, and manufacturing processes so that the final product satisfies quality requirements. Current study can be extended for various non-Newtonian fluids by utilizing entropy generation, porous medium, joule heating, etc.

NOMENCLATURE

x, y, z	*Cartesian Coordinates*
u, v, w	*Velocity Components*
ν	*Kinematic Viscosity*
U_∞	*Free Stream*
σ	*Electrical Conductivity*
B_0	*Magnetic Field Intensity*
ρ	*Density*
k_1	*Thermal Conductivity*
β	*Casson Fluid*
T	*Temperature*
$(\rho C_p)_p$	*Specific Heat at Constant Pressure*
D_T	*Thermophoretic Diffusion Coefficient*
T_∞	*Ambient Temperature*
D_B	*Brownian Diffusion Coefficient*
C	*Concentration*
K_r	*Chemical Reaction*
C_∞	*Ambient Concentration*
ζ	*Similarity Variable*
a,b	*Constants*
Θ	*Dimensionless Temperature*
T_w	*Wall Temperature*
Φ	*Dimensionless Concentration*
C_w	*Wall Concentration*
f	*Dimensionless Velocity in x-direction*
g	*Dimensionless Velocity in y-direction*
M	*Magnetic Parameter*
λ	*Free Stream Velocity*
PR	*Permeability Parameter*
Pr	*Prandtl Number*
Nb	*Brownian Motion*
Nt	*Thermophoresis Parameter*
Q	*Heat Generation*
Le	*Lewis Number*
CR	*Dimensionless Chemical Reaction*
TB	*Thermal Biot Number*
CB	*Concentration Biot Number*
Sh_x	*Sherwood Number*
Nu_x	*Nusselt Number*
Cf_y	*Skin Friction in y-direction*
Cf_x	*Skin Friction in x-direction*
Re_x	*Reynolds Number*
c	*Stretching Ratio Parameter*
$(\rho C_p)_f$	*Heat capacity of the fluid*

Abbreviations

O.D.E's	*Ordinary Differential Equations*
P.D.E's	*Partial Differential Equations*
MWCNT	*Multi Walled Carbon Nanotubes*
CFD	*Computational Fluid Dynamics*
MHD	*Magnetohydrodynamics*
RKF45	*Runge Kutta Fehlberg forth-fifth*

AUTHORSHIP CONTRIBUTIONS

Authors equally contributed to this work.

DATA AVAILABILITY STATEMENT

The authors confirm that the data that supports the findings of this study are available within the article. Raw data that support the finding of this study are available from the corresponding author, upon reasonable request.

CONFLICT OF INTEREST

The authors declared no potential conflicts of interest with respect to the research, authorship, and/or publication of this article.

ETHICS

There are no ethical issues with the publication of this manuscript.

REFERENCES

[1] Choi SUS, Eastman JA. Enhancing thermal conductivity of fluids with nanoparticles. Proceedings of ASME International Mechanical Engineering Congress & Exposition, November 12-17, 1995, San Francisco, CA.pp. 99-105.

[2] Buongiorno J. Convective transport in nanofluids. ASME J Heat Transf 2006;128:240-250. [CrossRef]

[3] Khan WA, Pop I. Boundary-layer flow of a nanofluid past a stretching sheet. Int J Heat Mass Transf 2010;53:2477-2483. [CrossRef]

[4] Hayat T, Kiyani MZ, Alsaedi A, Khan MI, Ahmad I. Mixed convective three-dimensional flow of Williamson nanofluid subject to chemical reaction. Int J Heat Mass Transf 2018;127:422-429. [CrossRef]

[5] Khan WA, Culham JR, Khan ZH, Pop I. Triple diffusion along a horizontal plate in a porous medium with convective boundary condition. Int J Therm Sci 2014;86:60-67. [CrossRef]

[6] Usman M, Soomro FA, Haq RU, Wang W, Defterli O. Thermal and velocity slip effects on Casson nanofluid flow over an inclined permeable stretching cylinder via collocation method. Int J Heat Mass Transf 2018;122:1255-1263. [CrossRef]

[7] Khan WA, Makinde OD, Khan ZH. Non-aligned MHD stagnation point flow of variable viscosity nanofluids past a stretching sheet with radiative heat. Int J Heat Mass Transf 2016;96:525-534. [CrossRef]

[8] Nagaraja KV, Khan U, Madhukesh JK, Hassan AM, Prasannakumara BC, Ben Kahla N, et al. Heat and mass transfer analysis of assisting and opposing

radiative flow conveying ternary hybrid nanofluid over an exponentially stretching surface. Sci Rep 2023;13:14795. [CrossRef]
[9] Karthik K, Madhukesh JK, Kiran S, Nagaraja KV, Prasannakumara BC, Gültekin F. Impacts of thermophoretic deposition and thermal radiation on heat and mass transfer analysis of ternary nanofluid flow across a wedge. Int J Model Simul 2024;1-13. [CrossRef]
[10] Reddy PS, Sreedevi P, Chamkha AJ. Hybrid nanofluid heat and mass transfer characteristics over a stretching/shrinking sheet with slip effects. J Nanofluids 2023;12:251-260. [CrossRef]
[11] Asalekar AJ, Sastry DR, Reddy MS, Barewar SD. Analysis of thermophysical properties of novel hybrid nanoparticles based vegetable nanofluid. J Therm Eng 2023;9:1466-1477. [CrossRef]
[12] Mebarek-Oudina F, Preeti, Sabu AS, Vaidya H, Lewis RW, Areekara S, et al. Hydromagnetic flow of magnetite-water nanofluid utilizing adapted Buongiorno model. Int J Mod Phys B. 2024;38:2450003. [CrossRef]
[13] Sheikholeslami M, Khalili Z. Simulation for impact of nanofluid spectral splitter on efficiency of concentrated solar photovoltaic thermal system. Sustain Cities Soc 2024;101:105139. [CrossRef]
[14] Jayadevamurthy PGR, Rangaswamy NK, Prasannakumara BC, Nisar KS. Emphasis on unsteady dynamics of bioconvective hybrid nanofluid flow over an upward-downward moving rotating disk. Numer Methods Partial Differ Equ 2024;40:e22680. [CrossRef]
[15] Sepehrnia M, Mohammadzadeh K, Rozbahani MH, Ghiasi MJ, Amani M. Experimental study, prediction modeling, sensitivity analysis, and optimization of rheological behavior and dynamic viscosity of 5W30 engine oil based SiO_2/MWCNT hybrid nanofluid. Ain Shams Eng J 2024;15:102257. [CrossRef]
[16] Alqahtani AM, Bilal M, Usman M, Alsenani TR, Ali A, Mahmuod SR. Heat and mass transfer through MHD Darcy Forchheimer Casson hybrid nanofluid flow across an exponential stretching sheet. ZAMM 2023:e202200213. [CrossRef]
[17] Puneeth V, Khan MI, Narayan SS, El-Zahar ER, Guedri K. The impact of the movement of the gyrotactic microorganisms on the heat and mass transfer characteristics of Casson nanofluid. Waves Random Complex Media 2022:1-24. [CrossRef]
[18] Akaje TW, Olajuwon BI, Musiliu Tayo RAJI. Computational analysis of the heat and mass transfer in a Casson nanofluid with a variable inclined magnetic field. Sigma 2023;41:512-523. [CrossRef]
[19] Seethamahalakshmi V, Rekapalli L, Rao TS, Santoshi PN, Reddy GVR, Oke AS. MHD slip flow of upper-convected Casson and Maxwell nanofluid over a porous stretched sheet: impacts of heat and mass transfer. CFD Lett 2024;16:96-111. [CrossRef]
[20] Lund LA, Asghar A, Rasool G, Yashkun U. Magnetized Casson SA-hybrid nanofluid flow over a permeable moving surface with thermal radiation and Joule heating effect. Case Stud Therm Eng 2023;50:103510. [CrossRef]
[21] Ali MY, Reza-E-Rabbi S, Ahmed SF, Nabi MN, Azad AK, Muyeen SM. Hydromagnetic flow of Casson nano-fluid across a stretched sheet in the presence of thermoelectric and radiation. Int J Thermofluids 2024;21:100484. [CrossRef]
[22] Kumar YS, Hussain S, Raghunath K, Ali F, Guedri K, Eldin SM, et al. Numerical analysis of magnetohydrodynamics Casson nanofluid flow with activation energy, Hall current and thermal radiation. Sci Rep 2023;13:4021. [CrossRef]
[23] Goyal R, Vinita, Sharma N, Bhargava R. GFEM analysis of MHD nanofluid flow toward a power-law stretching sheet in the presence of thermodiffusive effect along with regression investigation. Heat Transf 2021;50:234-256. [CrossRef]
[24] Makkar V, Hayat T, Alsaedi A. A mathematical simulation of unsteady MHD Casson nanofluid flow subject to the influence of chemical reaction over a stretching surface: Buongiorno's model. Heat Transf 2021;50:8640-8655. [CrossRef]
[25] Rajak U, Nashine P, Chaurasiya PK, Verma TN. A numerical investigation of the species transport approach for modeling of gaseous combustion. J Therm Eng 2021;7:2054-2067. [CrossRef]
[26] Rajak U, Panchal M, Allamraju KV, Nashine P, Verma TN, Pugazhendhi A. A numerical investigation on a diesel engine characteristic fuelled using 3D CFD approach. Fuel 2024;368:131488. [CrossRef]
[27] Shateyi S. Numerical analysis of three-dimensional MHD nanofluid flow over a stretching sheet with convective boundary conditions through a porous medium. In: Kandelousi MS, ed. Nanofluid Heat and Mass Transfer in Engineering Problems. Intech Open; 2017. [CrossRef]
[28] Khan JA, Mustafa M, Hayat T, Alsaedi A. Three-dimensional flow of nanofluid over a non-linearly stretching sheet: An application to solar energy. Int J Heat Mass Transf 2015;86:158-164. [CrossRef]
[29] Sulochana C, Ashwinkumar GP, Sandeep N. Similarity solution of 3D Casson nanofluid flow over a stretching sheet with convective boundary conditions. J Niger Math Soc 2016;35:128-141. [CrossRef]
[30] Hussain A, Malik MY, Salahuddin T, Bilal S, Awais M. Combined effects of viscous dissipation and Joule heating on MHD Sisko nanofluid over a stretching cylinder. J Mol Liq 2017;231:341-352. [CrossRef]
[31] Wang CY. Free convection on a vertical stretching surface. ZAMM 1989;69:418-420. [CrossRef]
[32] Mabood F, Khan WA, Ismail AM. MHD boundary layer flow and heat transfer of nanofluids over a nonlinear stretching sheet: a numerical study. J Magn Magn Mater 2015;374:569-576. [CrossRef]